De, Swarnalok; Nguyen, Hoang M.; Liljeström, Ville; Mäkinen, Kristiina; Kostiainen, Mauri; Vapaavuori, Jaana

Potato virus A particles – A versatile material for self-assembled nanopatterned surfaces

Published in:
Virology

DOI:
10.1016/j.virol.2022.11.010

Published: 01/01/2023

Document Version
Publisher's PDF, also known as Version of record

Virology 578 (2023) 103–110

Contents lists available at ScienceDirect

Virology

journal homepage: www.elsevier.com/locate/virology

Potato virus A particles – A versatile material for self-assembled nanopatterned surfaces

Swarnalok De [a], Hoang M. Nguyen [a], Ville Liljeström [b], Kristiina Mäkinen [c], Mauri A. Kostiainen [d,*], Jaana Vapaavuori [a,**]

[a] Department of Chemistry and Materials Science, Aalto University, 00076, Espoo, Finland
[b] Nanomicroscopy Center, OtaNano, Aalto University, 00076, Espoo, Finland
[c] Department of Microbiology, University of Helsinki, 00014, Helsinki, Finland
[d] Department of Bioproducts and Biosystems, Aalto University, 00076, Espoo, Finland

ARTICLE INFO

Keywords:
Potato virus A
Self-assembly
Virus nanoparticles
Bio-templates
Liquid crystal
Nanopatterning

ABSTRACT

Potato virus A (PVA) is a plant-infecting RNA virus that produces flexible particles with a high aspect ratio. PVA has been investigated extensively for its infection biology, however, its potential to serve as a nanopatterning platform remains unexplored. Here, we study the liquid crystal and interfacial self-assembly behavior of PVA particles. Furthermore, we generate nanopatterned surfaces using self-assembled PVA particles through three different coating techniques: drop-casting, drop-top deposition and flow-coating. The liquid crystal phase of PVA solution visualized by polarized optical microscopy revealed a chiral nematic phase in water, while in pH 8 buffer it produced a nematic phase. This allowed us to produce thin films with either randomly or anisotropically oriented cylindrical nanopatterns using drop-top and flow-coating methods. Overall, this study explores the self-assembly process of PVA in different conditions, establishing a starting point for PVA self-assembly research and contributing a virus-assisted fabrication technique for nanopatterned surfaces.

1. Introduction

Self-assembly of nanoparticles into organized structures has demonstrated its potential to benefit various technical fields, including electronics (Fendler, 2001), optics (Murphy et al., 2005), sensing (Thorkelsson et al., 2015), energy storage (Frey et al., 2009), and biomedical applications (Thanh and Green, 2010). Precise control over the self-assembly process relies upon the structural properties and the surface chemistry of the unit blocks, as well as the external conditions during the process (Linko et al., 2022). In general, bottom-up fabrication methods can offer an alternative route to overcome the challenge of top-down photolithography in producing high spatial resolution patterns at low cost (Nie and Kumacheva, 2008). Over the last two decades, virus nanoparticles (VNPs) have attracted focused attention and emerged as promising candidates for nanotechnology applications, including nanopatterning (Pokorski and Steinmetz, 2011; Korpi et al., 2020). As a component, when compared to the more commonly employed synthetic self-assembling materials such as block copolymers, VNPs provide superior assembly properties due to their uniform size, available surface functionalization possibilities, stability, and inexpensive purification on a large scale (Lee et al., 2009).

VNPs come in various symmetrical shapes, including rod-like and spherical structures, as well as a broad range of sizes ranging from 10 nm to a few microns. At the laboratory scale, VNPs can be prepared in milligram to gram-level quantities with high uniformity in composition, shape, and size (Pokorski and Steinmetz, 2011). The protein shell of VNPs, known as the capsid, acts as a protective layer for the genome and enables VNPs to resist temperature and pH changes. Since the capsid consists of several protein subunits that can be covalently or non-covalently bonded with a large variety of functional groups, VNPs provide various surface modification and functionalization opportunities (Smith et al., 2013; Chen et al., 2016; Kostiainen et al., 2013; Liljeström et al., 2017). Therefore, VNPs have been expandingly engineered for tissue engineering (Zhao et al., 2015), drug delivery (Chung et al., 2020; Esfandiari et al., 2016), and vaccine design (Plummer and Manchester, 2011; Sulczewski et al., 2018). In the context of nanoscale

* Corresponding author.
** Corresponding author.
E-mail addresses: mauri.kostiainen@aalto.fi (M.A. Kostiainen), jaana.vapaavuori@aalto.fi (J. Vapaavuori).

https://doi.org/10.1016/j.virol.2022.11.010
Received 23 September 2022; Received in revised form 16 November 2022; Accepted 22 November 2022
Available online 26 November 2022

patterning, generating a thin film of well-organized VNPs on a solid substrate remains challenging. Drop-casting (Tseng et al., 2006; Wargacki et al., 2008), spin-coating (Rink et al., 2017), and dip-coating (Yoo et al., 2011; Atanasova et al., 2015) are the most common methods for depositing VNPs. To obtain a stable film, a substantial electrostatic attraction between VNPs and substrate is usually required (Rong et al., 2011). However, this can lead to low ordering of the VNP patterns due to the initial strong electrostatic interaction with the substrate, leading to kinetically trapped structures (Knez et al., 2004; Lee et al., 2007). Furthermore, the coffee ring (Kaliyaraj Selva Kumar et al., 2020) and the edge effects (Puetz and Aegerter, 2004) associated with the above-mentioned coating techniques hamper the preparation of uniform structures and make them less appealing.

Most studies on the self-assembly of rod-like VNPs have been limited to tobacco mosaic virus (TMV) and M13 bacteriophage. The self-assembly of TMV (18 nm in width × 300 nm in length) has been known as a head-to-tail assembly process, in which the dipolar ends of the TMV's helical structure interact hydrophobically and complementarily with each other (Rong et al., 2011; Niu et al., 2006; Bruckman et al., 2007). Specifically, an acidic environment with pH of less than 4 was shown to promote the self-assembly of TMV into a fiber-like structure by reducing the repulsive carboxylate interaction (Santos et al., 2004; Lu et al., 1996). M13 (6 nm in width × 880 nm in length) is another standard model for the study of rod-like VNPs self-assembly. The lyotropic LC behavior of M13 is the reason behind its highly ordered organization (Park et al., 2021; Lee et al., 2003; Chung et al., 2011). In addition, different complex liquid crystal (LC) structures have been shown as a function of evaporation (Park et al., 2021), concentration (Lee et al., 2003), or the interplay between meniscus constraints and material flux during the coating process of dip-coated M13 films (Chung et al., 2011).

Unlike rigid rod-like TMV and semi-rigid M13, potato virus A (PVA) has a highly flexible structure, which can provide diverse opportunities for self-assembled patterns. PVA belongs to the genus *Potyvirus*, which is considered a primary plant pathogen family from an economic perspective (Valli et al., 2015). PVA VNPs can be prepared *in planta* with high reproducibility and uniform dimensions (Valli et al., 2015). They obtain a flexuous rod-like structure with a high aspect ratio, typically 680–900 nm in length and 11–13 nm in width (Martínez-Turiño and García, 2020). Their capsid comprises approximately 2000 protein subunits enclosing the genomic RNA (Martínez-Turiño and García, 2020), in which the exposed N-terminus can tolerate small amino acid insertion (Martí et al., 2022). Analogously to other VNPs, the exposed amino acid side chains in the capsid layer of PVA allow versatile chemical modification and functionalization. PVA is an extensively studied potyvirus and the number of the research works is constantly increasing, yet most have focused on the general biological aspects. Though there are few reports available on surface and structural characterization of PVA (Nault et al., 2015; Ksenofontov et al., 2018; Shtykova et al., 2021), the only applicative aspect of PVA that has been studied is as enzyme nanocarriers (Besong-Ndika et al., 2016).

Here, we expand the use of PVA and report on their self-assembly behaviour and utilization for surface nanopatterning. In order to be feasible, relatively large amounts of PVA VNPs need to be produced. We show the optimization of the purification process based on a pre-existed protocol developed by Gabrenaite-Verkhovskaya et al. (2008) Compared to the previous protocol, PVA VNPs with better quality and higher yield are obtained, and we discuss their stability with different pHs, buffer strengths, added salts as well as concentrations. The self-assembly of PVA in water and buffer solution results in liquid crystalline (LC) behavior and a model was developed to explain the effect of surface charge on the orientation of nanoparticles. Thin films of PVA with varied surface morphologies could be deposited onto a substrate by drop-top or flow-coating methods. These methods are discussed in detail regarding their feasibility and applicability. It should be noted that self-assembly of VNPs in this article refers exclusively to intermolecular self-assembly of VNPs. This work provides a straightforward pathway for generating surface patterns, expanding the knowledge of nanoparticle self-assembly to a new type of VNPs.

2. Experimental section

2.1. PVA VNP purification protocol

PVA VNPs were produced in *Nicotiana benthamiana* plants (NCBI: txid4100). The plants were grown at 22 °C under 16 h (light) and 8 h (dark) photoperiod in environmentally controlled greenhouses. Young plants at the 4-leaves stage were infected with *Agrobacterium* carrying PVA infectious complementary DNA (icDNA). The infections were then allowed to spread systemically for three weeks. Infected leaves were then harvested and stored at −80 °C. Full length infectious PVA VNPs were subsequently purified from the infected leaves following the protocol described in Fig. S1.

2.2. PVA stability assay

PVA samples of concentration 5×10^{11} particles/μL were mixed with test subjects (pH, buffers, or salts) of desired molarities. Samples were incubated at room temperature for 96 h. After the incubation, cDNA was prepared from the particles using the H Minus First Strand cDNA synthesis kit (Product No. K1632, Thermo Fisher Scientific) with random hexamer primers. The particle concentration was further quantified via qPCR using a Maxima SYBR Green qPCR Master mix (Thermo Fisher Scientific) and a CFX96 TouchTM Real-Time PCR Detection System. PVA RNA quantification was carried out by amplifying the coat protein (CP) region of PVA RNA using primers-forward- 5′-CAT GCC CAG GTA TGG TCT TC-3′, reverse- 5′-ATC GGA GTG GTT GCA GTG AT-3'. Percentage stability was calculated by comparing incubated particle quantity with control particles (cDNA prepared at 0 h).

2.3. PVA particle visualization

PVA particles and self-assembled structures were visualized using a Tescan Mira 3 scanning electron microscope (SEM); a Bruker Multimode 8 (Bruker) atomic force microscope (AFM) in non-contact mode using Silicon tips (NCHV-A, Bruker); and Jeol JEM-1400 and JEM-2800 transmission electron microscopes (TEM). α-CP antibody was coated on the TEM grid surface by incubating the carbon surface of the grid with the antibody at 1:100 dilution for 1 h at room temperature.

2.4. PVA liquid crystal analysis

Liquid crystal domains of PVA were visually analyzed using an Olympus BX53 M polarized optical microscope (POM).

Small and wide-angle X-ray scattering (SAXS, WAXS) data is obtained using a Xenocs Xeuss 3.0 SAXS/WAXS system (Xenocs SAS, Grenoble, France). The system includes a microfocus X-ray source (sealed tube) with a Cu target and a multilayer mirror which yields a parallel beam with a nominal wavelength of 1.542 Å (combined Cu K-α_1 and Cu K-α_2 characteristic radiation). The source operates at 50 kV and 0.6 mA. The beam is collimated by a set of variable slits and the beam size at the sample was 0.4 mm during the experiment. The system does not include a beam stop, which enables direct measurement of sample transmission. The background scattering from sample holder is normalized and subtracted from the data according to sample transmission. The data is acquired using an area detector (Eiger2 R 1 M, Dectris AG, Switzerland) that was in the evacuated chamber. The sample-to-detector distance was calibrated by measuring the diffraction from a known LaB_6 standard sample.

The samples were sealed in borosilicate Mark tubes (diameter 1.5 mm, wall thickness 10 μm, Hilgenberg GmbH, Germany) using hot glue and the tubes were in the evacuated sample chamber during the

measurement (pressure <1 mBar). In addition, reference samples (empty Mark tube, solvent) were measured in the same conditions. Scattering contribution from the empty chamber, the capillary, and the solvent were sequentially subtracted from the azimuthally averaged data.

2.5. PVA concentration calculation

PVA concentration was measured and adjusted using Nanodrop Microvolume Spectrophotometer (ThermoScientific). A typical potyvirus extinction coefficient of 2.65 (A 0.1%, 1 cm at 260 nm) was considered while calculating PVA concentration (Cuenca et al., 2016).

2.6. In silico analysis of charge distribution of PVA CP in different pH

Predicted model of PVA CP (strain B11, GenBank accession number AJ296311) was generated using I-TASSER server for protein structure and function prediction. The charge distribution model of PVA CP was generated using the APBS-PDB2PQR software hosted by a server (https://server.poissonboltzmann.org/). The model was visualized using the software ChimeraX 1.2.5. Isoelectric pH (pI) of PVA CP and net charge of the CPs at different pH conditions were determined using online server PROTEIN CALCULATOR v3.4 hosted by http://protcalc.sourceforge.net/.

2.7. Drop-top coating method

First, the TEM grids were coated with primary antibody against PVA CP (α-CP, SASA, UK) by incubating the grids with 1:100 diluted Petri dish solution for 1 h. The grids were then washed to remove excess antibodies. Meanwhile, a 20 μL drop of 3–5 mg/mL PVA in water or buffer was allowed to rest for 5 min on a Petri dish placed over ice. A α-CP coated grid was then instantly placed on the top of the drop with the help of a tweezer and removed. Finally, the grid was washed on the top of a drop of water or buffer exhaustively to reveal the monolayer of PVA VNPs bound to the grid.

2.8. Statistical analysis

Statistical significances were calculated between the marked samples and their corresponding controls using Student's *t*-Test. Only those cases where the calculated *p*-values were below 0.05 ($p < 0.05$) were considered significantly different from control.

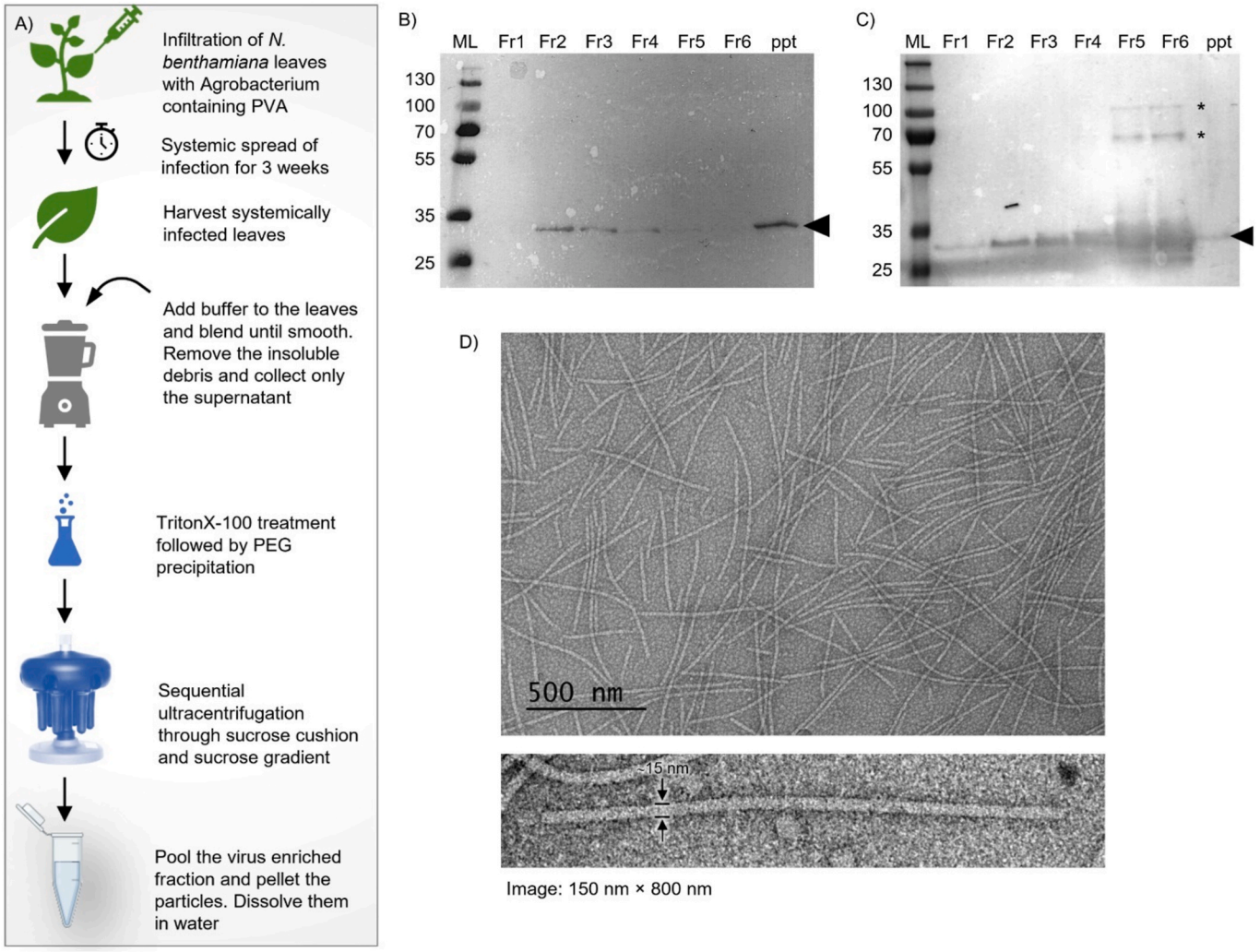

Fig. 1. Development of purification protocol for obtaining high-quality PVA particles suitable for material science applications. A) Schematic representation of the optimized purification protocol. B) Particle distribution in the old protocol. Fr1 – Fr6 denotes six consecutive 2 mL fractions collected from 5 to 40% sucrose gradient. C) Particle distribution in the new protocol. Arrowheads on the western blots (B and C) denote the position of monomeric PVA CP. In addition, Fr5 – Fr6 in C show faint bands near 70 and 100 kDa (marked with asterisk) supposedly coming from dimer and trimers of CP. D) TEM image of the purified particles.

3. Results and discussions

3.1. Purification of PVA VNPs

In order to employ PVA VNPs in material science applications, it is essential to obtain high-quality purified PVA VNPs with sufficiently high yield. Therefore, we developed further the protocol for PVA purification to suit this purpose. The protocol steps are presented in Fig. 1A. The existing protocol for PVA purification was reported in the work of Gabrenaite-Verkhovskaya et al. (2008) In their method, the particles were divided into two fractions, soluble fraction (F) and precipitated fraction (P2). The F-fraction mainly comprised broken/defective VNPs, while P2 fraction had mostly intact VNPs. However, we found that the P2-fraction contained co-precipitated impurities that were very difficult to eliminate. Earlier, Choi et al. (1977) reported that potyvirus turnip mosaic virus (TuMV) was also prone to aggregation with host-derived contaminants during purification and this was the single most critical reason behind the loss in the particle yield. To deal with this issue, we included a chelating agent EDTA, a dispersing agent NaOH and a reducing agent β-mercaptoethanol in sodium phosphate buffer (pH 7.4). Compared to the original protocol for purification (Fig. 1B), the new protocol significantly altered the distribution of PVA VNPs within the sucrose gradient (Fig. 1C). PVA coat protein (CP) bands in Fig. 1C clearly demonstrate that the particle concentrations gradually increased with increasing sucrose concentration, and the maximum amount was concentrated in fractions 5 and 6. The precipitate, on the other hand, was largely depleted of VNPs. VNPs concentrated from pooled fractions 5 and 6 were intact, of appropriate size, devoid of insoluble debris (Fig. 1D, see also Fig. S2) and suitable for subsequent studies.

3.2. Stability behavior of PVA VNPs

Though there are several studies on PVA biology, there lies a substantial knowledge gap in understanding the properties of PVA VNPs from a material science perspective. Our initial objective was to study the stability of PVA VNPs in different pH, buffer strengths, salts, and concentrations. Since RNA is highly unstable in room temperature solutions and no protective measures for stabilization of the viral RNA (vRNA) were employed, we assume that the remaining RNAs after the incubation period originated from intact PVA VNPs. Therefore, the RNA quantity can be used as a direct indicator of intact PVA quantity. Therefore, after 96 h of incubation at room temperature, we prepared complementary DNA (cDNA) from the PVA samples and calculated the percentage of remaining vRNA by comparing it with the cDNA samples prepared at 0 h. Considering RNA stability as a measure of particle stability, Fig. 2 reveals that the VNPs were the most stable at pH 8.8 and 9.5 (Fig. 2A) and low buffer/ionic concentration (Fig. 2B and C). The effect of all the salts tested here at 0.1 M had a negative impact on the particle stability, however the effect of divalent metal salts i.e., $CaCl_2$, $MgCl_2$, and $MnCl_2$ were more prominent (Fig. 2C and D).

3.3. PVA self-assembly behavior

Next, we studied the self-assembly behavior of PVA in water (PVA_{water}) and pH 8 buffer (PVA_{buffer}). As for buffer, we chose ammonium acetate buffer (0.1 M) to avoid the artifacts caused by the concentration and crystallization of salts (as compared to HEPES). Our drop-casting protocol consisted of dispensing a drop of 3 mg/mL PVA in either solvent onto a Si wafer and allowing it to dry (Fig. 3A). Then, we investigated the surface features of the resulting films using SEM and AFM. As observed through both of these methods, the surface of PVA_{water} film demonstrated bundles of multiple PVA VNPs arranged in all lateral directions (Fig. 3B,D). On the other hand, SEM and AFM images of PVA_{buffer} film surface revealed a parallelly arranged PVA particles (Fig. 3C,E) forming a relatively smooth film.

Each PVA particle is made up of approx. 2000 copies of coat proteins.

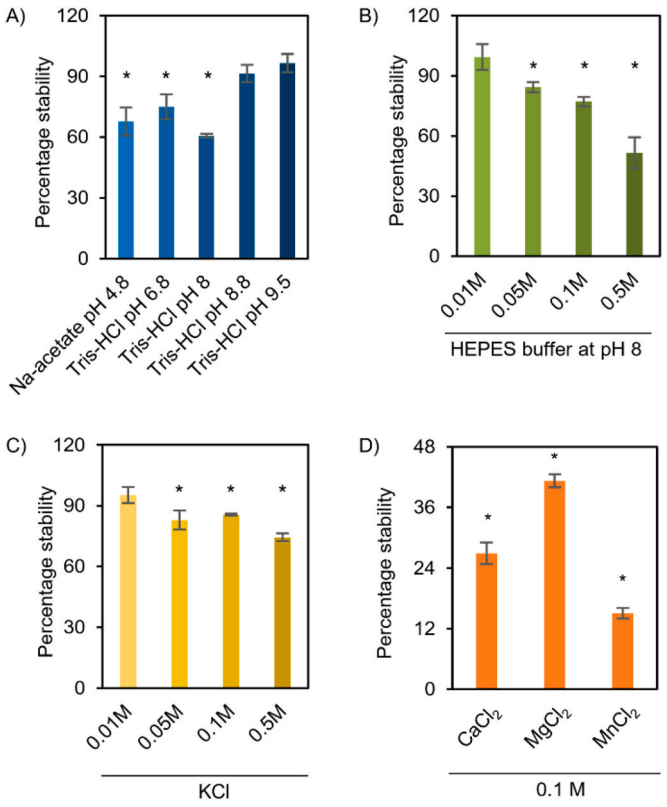

Fig. 2. Stability of PVA particles in different solution conditions. A) Stability in 0.1 M buffers with different pH. B) Different molarity of HEPES buffer at pH 8. C) Different ionic concentrations of KCl. D) Different salts at 0.1 M * denotes a significant difference ($p < 0.05$) from control.

Being proteinaceous in nature the VNPs carry positive and negative charge in buffer below and above pI respectively, while at pI the VNPs are neutral. As the structure of PVA VNPs are not yet resolved, we did an *in silico* modelling of PVA CP to visualize its charge distribution at different pHs (Fig. 3A). Calculated pI of PVA CP was predicted to be 7.02. Since the pH of deionized water is usually slightly below pH 7 and buffer was of pH 8, we then theoretically estimated net charges at pH 6, 7, and 8. Consistent with our assumption, the charges were 5.7, 0.1, and −2.7 units respectively (Fig. 3A).

We characterized the LC behavior of PVA_{water} and PVA_{buffer} by polarized optical microscope (POM) and small-angle x-ray scattering (SAXS), which are complementary methods as POM describes alignment on micrometer level and above whereas SAXS provides information about particle shape and packing in the 1–100 nm range (Dogic and Fraden, 2000).

Apart from the two PVA_{water} samples with a particle concentration of 50 mg/mL, the SAXS profiles of PVA_{water} and PVA_{buffer} samples correspond directly to the form factor $P(q)$ of the particles. Thus, according to SAXS, the structure of these samples was weakly correlated, or the correlation distance is larger than which can be observed with the SAXS instrument used. However, the PVA_{water} sample with the highest concentration shows clear deviation from $P(q)$, as a correlation maximum (a "shoulder" at small q) was observed, which indicates a periodic positional order (Fig. 4D and E). The correlation maximum represents the typical center-to-center distance d_{cc} in the lyotropic LC phase, hence these samples exhibited both orientational order (POM, discussed below) and positional order (SAXS). Moreover, the position of the correlation maximum (q ~0.012–0.014 $Å^{-1}$) translates to a d_{cc} of 45–52 nm. Here we assume that the rod-like virus had an effective density similar to that of water. Providing that the virus concentration was 50 mg/mL, this condition would yield a theoretical d_{cc} of 51 nm, which

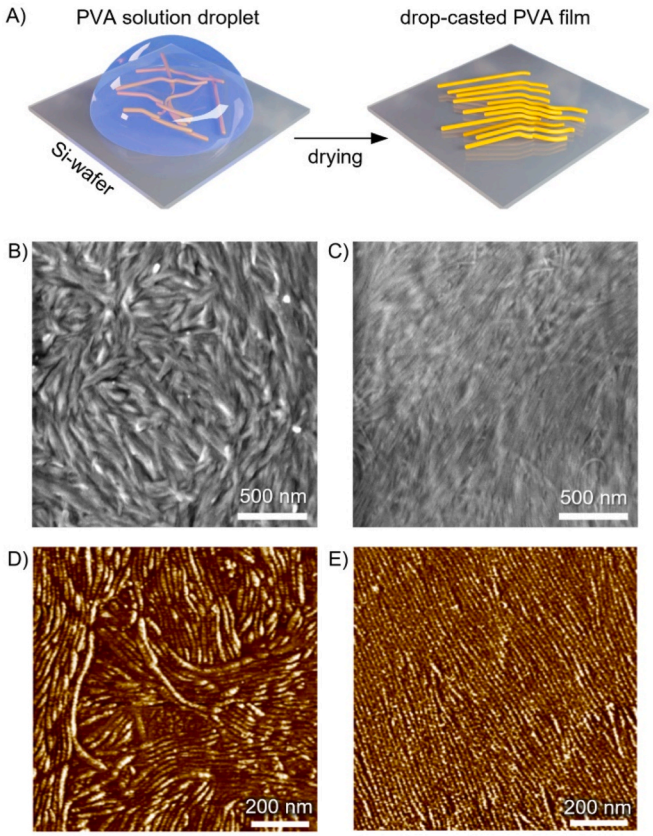

Fig. 3. Self-assembly behavior of drop-casted PVA films. A) Schematic illustration of the drop-casting of PVA solution (3 mg/mL) on Si wafer. B,C) SEM images of drop-casted PVA_{water} and PVA_{buffer} films, respectively. D,E) AFM images of drop-casted PVA_{water} and PVA_{buffer} film respectively.

corresponds to a continuous 2D close-packing of rods (Fig. S3a). This result is in strong agreement with an assumption of repulsion induced LC ordering. However, the underestimation of the unknown effective density makes this result slightly inaccurate. The effective density is most probably a little higher than that of water, which means that the theoretical d_{cc} of 51 nm should be higher.

According to POM, all samples exhibited local LC nematic ordering with orientational order (Figs. S3b and c). This conclusion is based on the observation that all samples showed bright areas when observed between crossed polarizers. In particular, POM images of PVA_{water} LC at 15 mg/mL concentration demonstrated clear signature of chiral nematic LC phase i.e., fingerprint like alternating bright and dark bands (Fig. 4B). (Dogic and Fraden, 2000) Higher magnification POM images reveal large alternating domains of bright and dark bands for PVA_{water} compared to thin filament-like continuous phase for PVA_{buffer} (Figs. S3b and c), which demonstrates the difference between their LC behaviour. Alternating bright and dark bands, *i.e.,* a "fingerprint pattern" is typical for a chiral nematic LC, where the director of the nematic phase alternates between being perpendicular to the direction of observation (bright area) and being parallel to the direction of observation (dark area). The pitch of the chiral nematic LC, which is double the period of the fingerprint, is more than 100 μm, meaning that the LC phase is not strongly twisted, thus d_{cc} is expected to be higher.

Also, PVA_{buffer} showed both bright and dark areas when observed between crossed polarizers (Fig. 4C and Fig. S3c). Interestingly, the characteristic domain size (area with uniform brightness) was less than 10 μm, showing that the alignment of the particles had no long-range correlation. Therefore, the local arrangement is more likely due to the high aspect ratio of the particles, rather than the long-range interaction.

Chiral nematic LC phase has earlier been reported for semi-flexible viruses like M13 and Fd phage (Dogic and Fraden, 2000). On the other hand, pH dependent transition of chiral nematic to nematic LCs at low and high pH has been reported for cellulose nanocrystals (CNCs). Electrostatic properties of the solution and their interaction with CNCs were deemed responsible for this phenomenon (Li et al., 2019). Previously, phenylboronic acid (PBA) functionalized M13 phage was shown to transit from chiral nematic LC to nematic LCs, based on whether the pH of the solution was above or below the pKa of PBA (Cao et al., 2014). In our case, compared to water, buffer at pH 8 could influence the charge distribution of the VNPs (positive to negative surface charge), electrostatic properties of the solution, and protonation of histidine (Pogostin et al., 2019). It is clear that the ionic strength of the solution affected the electrostatic repulsion between particles. Debye length λ_D, which is the characteristic range of electrostatic interaction in solution, strongly depends on the ionic strength. An ionic strength of 0.1 M would yield λ_D ~1 nm, and for pure water (ionic strength 10^{-7} M) $\lambda_D \sim 1$ μm. In other words, the electrostatics interactions were significant in pure water and minimal in buffer. The aforementioned factors play a role in differential LC behavior of PVA in water and buffer and are responsible for the LC behaviors behind contrasting self-assembly of PVA_{water} and PVA_{buffer} (Fig. 3B–E).

3.4. Translating PVA LCs to self-assembled nanopatterned thin film

As discussed earlier, top layer of PVA_{buffer} drop-casted films showed smooth and aligned stripe patterns consisting of individual concatenated PVA VNPs. We hypothesize that, as the droplets begins to evaporate, concentration of PVA partially increase in the surface of the drop where the effect of evaporation is higher. During this process adjacent VNPs assemble in the most favorable fashion, i.e., chiral nematic LC for PVA_{water} and nematic LC for PVA_{buffer}. In order to translate the LC assemblies from the droplet surface into solid state nanopatterned thin film, TEM grids coated with PVA α-CP antibody were utilized. This drop-top coating method is illustrated in Fig. 5A. The resulting PVA surface pattern from PVA_{water} and PVA_{buffer} samples were imaged with SEM, as shown in Fig. 5B–C. Consistent with our assumption, we observed in the PVA_{water} samples bundles of PVA in all directions (Fig. 5B). PVA_{buffer}, on the other, hand generated more directionally oriented PVA pattern (Fig. 5C).

We further washed the grids extensively to remove excess PVA from the grids to reveal the monolayer of PVA VNPs directly bound to the antibodies. Transmission electron microscopy (TEM) images of the PVA monolayer also agrees with our hypothesis. Owing to changing directors of the LC planes in PVA_{water}, the VNPs are pointing towards all in-plane directions (Fig. 5D, also see Fig. 4D). The FFT diffractogram (Fig. 5D inset) further confirms the isotropic assembly of PVA monolayer on the grid. Similarly, TEM image and FFT diffractogram for PVA_{buffer} also corroborates with our hypotheses and show anisotropic assembly of monolayer PVA via drop-top method (Fig. 5D). Though some misdirected VNPs could be seen across PVA monolayer, it could be attributed to imperfections in LC phases that got bound to the α-CP antibodies and could not be removed later even with extensive washes. We also validated that the anisotropic self-assembly behavior of PVA is a pH-dependent phenomenon by comparing the PVA monolayer morphologies from PVA dissolved in ammonium acetate/HEPES buffer at pH8 (Fig. S4).

3.5. Towards PVA-based biotemplating applications

Drop-top coating method successfully generated organized self-assembled structures with PVA_{buffer}, but its practical use could be limited due to difficult scale-up. Therefore, we explored flow-coating as an alternative self-assembly technique for organizing PVA VNPs over a larger surface. Earlier Moghimian et al. (2014) reported better alignment of M13 phage onto amorphous carbon surface (i.e., TEM grid) compared to SiO_2 surface. The method applied therein comprised initial

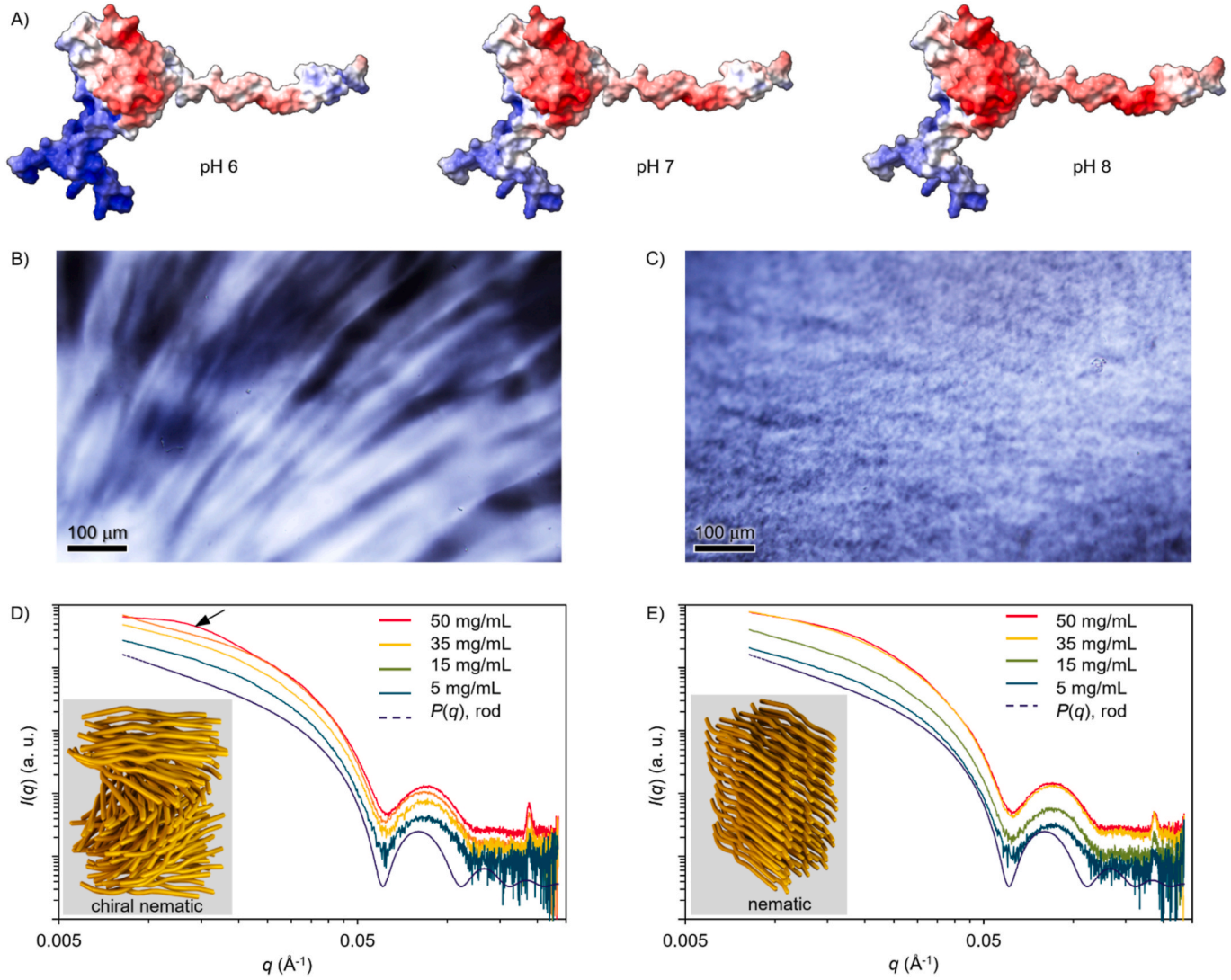

Fig. 4. Analysis of PVA self-assembly behavior in water and buffer. A) PVA CP charge distribution in different pHs. Since the structure of PVA particles is not yet resolved in atomic detail, we predicted the structure of PVA CP using I-TASSER. Charge distribution was calculated using APBS-PDB2PQR software. Color code: blue, white and red denotes positive, neutral and negative charges respectively. B) LC behavior of 15 mg/mL PVA_{water} visualized by POM. C) LC behavior of 15 mg/mL PVA_{buffer} visualized by POM. Scale bars represents 100 μm. D,E) SAXS profile for PVA in water and buffer respectively. The dashed line represents a theoretical model of *P(q)* for a flexible cylinder with radius 6.3 nm, length 400 nm, and Kuhn length 30 nm generated using SasView 4.2.0 software. The arrow indicates the position of the correlation peak.

adsorption of M13 particles onto substrate surface followed by washing at an angle of 45°. In our study, we coated Si-wafer surface with 20 nm carbon film via spluttering. Then we dispensed PVA_{buffer} along the carbon coated surface as described in Fig. 6A. The substrate here was devoid of α-CP antibodies to bind the VNPs, and the contact time of the solution to the surface was minimum due to vertical flow. Therefore, higher concentration (15 mg/mL) of PVA_{buffer} was used in this study to ensure retention of sufficient amount of PVA VNPs on the substrate. Moreover, since PVA_{buffer} showed nematic LC phase at 15 mg/mL range (Fig. 4C), it was deemed as a good concentration for depositing aligned PVA VNPs even with low contact time. The PVA deposition pattern on the surface was analyzed with AFM, which demonstrated the formation of a periodic surface pattern with local alignment (Fig. 6B). These results are thus aligned with the results done earlier with filamentous M13 particles (Moghimian et al., 2014) and highlight the importance of both solution-state self-assembly of the VNPs and the interactions between the deposition substrate and the VNPs in question for the final thin film morphology.

When taking into account all the conducted nanopatterning experiments, all the three coating methods including drop-casting, drop-top deposition and flow-coating offer ways for creation of relatively smooth aligned in-plane cylindrical nanopatterns. Out of these methods, drop-top and flow coating arguably enable better control over thin film thickness and are more suitable for different types of layer-by-layer applications, as compared to drop-casting, which may also suffer from thickness variations due to coffee ring effects. Furthermore, when comparing drop-top deposition against flow-coating, the latter opens up wider opportunities in terms of tunability and scalability.

4. Conclusions

The PVA purification process presented in this work is superior to the previously reported protocols. By adding chelating (EDTA), dis-aggregating (NaOH), and reducing agents (β-mercaptoethanol) to the PVA solution, we were able to obtain higher yield of intact PVA VNPs, which is an important factor for all down-stream applications. The produced PVA particles were the most stable in low ionic-concentrated buffers with pH > 8, and without the addition of salts.

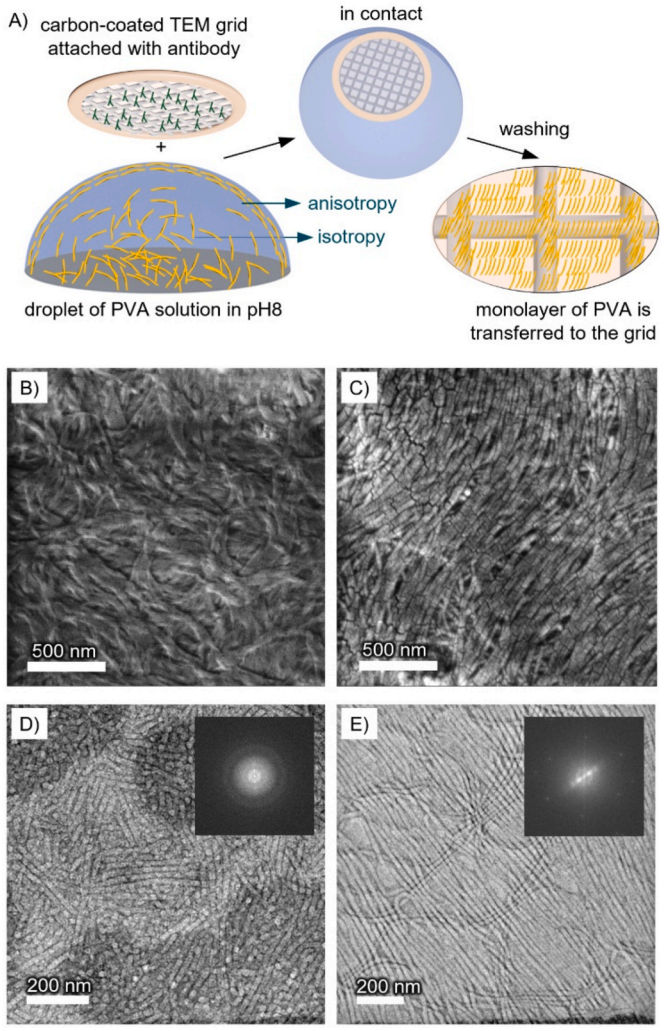

Fig. 5. PVA templating using drop-top coating method. A) Schematic model depicting drop-top coating method. B,C) SEM image of the PVA particles bound to the grid right after they were removed from the top of the corresponding drops in PVA_{water} and PVA_{buffer} respectively. D,E) TEM images of the PVA monolayer after extensive washing of PVA monolayer bound to the grid by α-CP antibody. Insets show FFT diffractograms produced by (D) isotropic PVA_{water} and (E) anisotropic PVA_{buffer}.

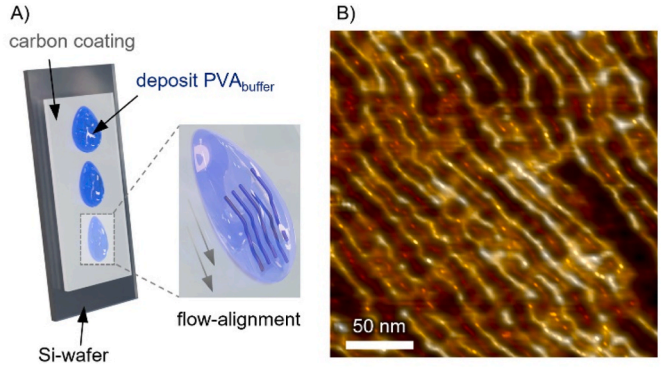

Fig. 6. Organization of PVA VNPs by flow-coating method. A) Schematic representation of the flow-coating method. Organized assembly of PVA VNPs could be seen in (B) AFM image.

Investigation on the LC behavior of PVA suggested that the organization of particles in water was affected by the electrostatic repulsion between particles, leading to a chiral nematic phase, and thus patterns of isotropic orientation were obtained in the drop-casted film after drying. In contrast, buffer with a pH above isoelectric point resulted in pure nematic phase dominated by entropic alignment, therefore creating a drop-casted film with anisotropic morphology. Self-assembled thin films with aligned nanopatterns could also be achieved with drop-top and flow-coating methods. The presented investigation on the self-assembly of PVA as well as their applicability in thin film deposition contribute towards the development of novel VNP nanostructures. As compared to nanopatterning with synthetic block copolymers, with PVA VNPs, similar pattern dimensions can be reached combined with more versatile possibilities for controlled surface functionalization. Thus, these materials provide an unexplored platform for fabricating highly controlled nanoscale organic-inorganic functional materials and devices.

CRediT authorship contribution statement

Swarnalok De: Funding acquisition, Conceptualization, Methodology, Investigation, Writing – original draft. **Hoang M. Nguyen:** Formal analysis, Methodology, Investigation, Writing – original draft. **Ville Liljeström:** Formal analysis, Methodology, Writing – review & editing. **Kristiina Mäkinen:** Supervision, Funding acquisition, Writing – review & editing. **Mauri A. Kostiainen:** Funding acquisition, Supervision, Writing – review & editing. **Jaana Vapaavuori:** Funding acquisition, Supervision, Project administration, Writing – review & editing.

Declaration of competing interest

The authors declare no conflict of interest.

Acknowledgment

The research in Multifunctional Material Design lab (Aalto University) was funded by The Ella Georg Ehrnrooth Foundation, the European Research Council (H2020) StG "Autonomously adapting and communicating modular textiles" No. 949648 ModelCom, Academy of Finland SUPER-WEAR project (decision number: 322214), ProCrystal (decision 680210), Academy of Finland's Flagship Programme under Projects No. 318890 and 318891 (Competence Center for Materials Bioeconomy, FinnCERES). Research in the Mäkinen lab (University of Helsinki) is supported by Academy of Finland (decision 332950).

Further, we acknowledge OtaNano Nanomicroscopy Center at Aalto University for their facilities and expertise that were crucial for the SAXS and TEM studies carried out in this work. We also Acknowledge HiLIFE Biocomplex unit at the University of Helsinki, a member of Instruct-ERIC Centre Finland, FINStruct, and Biocenter Finland for their facilities and expertise that were crucial for the purification of PVA VNPs.

Appendix A. Supplementary data

Supplementary data to this article can be found online at https://doi.org/10.1016/j.virol.2022.11.010.

References

Atanasova, P., Stitz, N., Sanctis, S., Maurer, J.H.M., Hoffmann, R.C., Eiben, S., Jeske, H., Schneider, J.J., Bill, J., 2015. Genetically improved monolayer-forming tobacco mosaic viruses to generate nanostructured semiconducting bio/inorganic hybrids. Langmuir 31 (13), 3897–3903. https://doi.org/10.1021/acs.langmuir.5b00700.

Besong-Ndika, J., Wahlsten, M., Cardinale, D., Pille, J., Walter, J., Michon, T., Mäkinen, K., 2016. Toward the reconstitution of a two-enzyme cascade for resveratrol synthesis on potyvirus particles. Front. Plant Sci. 7 (FEB2016), 89. https://doi.org/10.3389/fpls.2016.00089.

Bruckman, M.A., Niu, Z., Li, S., Lee, L.A., Varazo, K., Nelson, T.L., Lavigne, J.J., Wang, Q., 2007. Development of nanobiocomposite fibers by controlled assembly of

rod-like tobacco mosaic virus. NanoBiotechnology 3 (1), 31–39. https://doi.org/10.1007/s12030-007-0004-4.
Cao, J., Liu, S., Xiong, J., Chen, Y., Zhang, Z., 2014. Stimuli responsive chiral liquid crystal phases of phenylboronic acid functionalized rodlike viruses and their interaction with biologically important diols. Chem. Commun. 50 (72), 10402–10405. https://doi.org/10.1039/c4cc04639k.
Chen, Z., Li, N., Li, S., Dharmarwardana, M., Schlimme, A., Gassensmith, J.J., 2016. Viral chemistry: the chemical functionalization of viral architectures to create new technology. Wiley Interdiscip. Rev. Nanomedicine Nanobiotechnology 8 (4), 512–534. https://doi.org/10.1002/wnan.1379.
Choi, J.K., Maeda, T., Wakimoto, S., 1977. An improved method for purification of turnip mosaic virus. Japanese J. Phytopathol. 43 (4), 440–448. https://doi.org/10.3186/jjphytopath.43.440.
Chung, W.J., Oh, J.W., Kwak, K., Lee, B.Y., Meyer, J., Wang, E., Hexemer, A., Lee, S.W., 2011. Biomimetic self-templating supramolecular structures. Nature 478 (7369), 364–368. https://doi.org/10.1038/nature10513.
Chung, Y.H., Cai, H., Steinmetz, N.F., 2020. Viral nanoparticles for drug delivery, imaging, immunotherapy, and theranostic applications. Adv. Drug Deliv. Rev. 156, 214–235. https://doi.org/10.1016/j.addr.2020.06.024.
Cuenca, S., Mansilla, C., Aguado, M., Yuste-Calvo, C., Sánchez, F., Sánchez-Montero, J. M., Ponz, F., 2016. Nanonets derived from turnip mosaic virus as scaffolds for increased enzymatic activity of immobilized Candida Antarctica lipase B. Front. Plant Sci. 7 (APR2016), 464. https://doi.org/10.3389/fpls.2016.00464.
Dogic, Z., Fraden, S., 2000. Cholesteric phase in virus suspensions. Langmuir 16 (20), 7820–7824. https://doi.org/10.1021/la000446t.
Esfandiari, N., Arzanani, M.K., Soleimani, M., Kohi-Habibi, M., Svendsen, W.E., 2016. A new application of plant virus nanoparticles as drug delivery in breast cancer. Tumor Biol. 37 (1), 1229–1236. https://doi.org/10.1007/s13277-015-3867-3.
Fendler, J.H., 2001. Chemical self-assembly for electronic applications. Chem. Mater. 13 (10), 3196–3210. https://doi.org/10.1021/cm010165m.
Frey, N.A., Peng, S., Cheng, K., Sun, S., 2009. Magnetic nanoparticles: synthesis, functionalization, and applications in bioimaging and magnetic energy storage. Chem. Soc. Rev. 38 (9), 2532–2542. https://doi.org/10.1039/b815548h.
Gabrenaite-Verkhovskaya, R., Andreev, I.A., Kalinina, N.O., Torrance, L., Taliansky, M. E., Mäkinen, K., 2008. Cylindrical inclusion protein of potato virus A is associated with a subpopulation of particles isolated from infected plants. J. Gen. Virol. 89 (3), 829–838. https://doi.org/10.1099/vir.0.83406-0.
Kaliyaraj Selva Kumar, A., Zhang, Y., Li, D., Compton, R.G., 2020. A mini-review: how reliable is the drop casting technique? Electrochem. Commun. 121, 106867 https://doi.org/10.1016/j.elecom.2020.106867.
Knez, M., Sumser, M.P., Bittner, A.M., Wege, C., Jeske, H., Hoffmann, D.M.P., Kuhnke, K., Kern, K., 2004. Binding the tobacco mosaic virus to inorganic surfaces. Langmuir 20 (2), 441–447. https://doi.org/10.1021/la035425o.
Korpi, A., Anaya-Plaza, E., Välimäki, S., Kostiainen, M., 2020. Highly ordered protein cage assemblies: a toolkit for new materials. Wiley Interdiscip. Rev. Nanomedicine Nanobiotechnology 12 (1), e1578. https://doi.org/10.1002/wnan.1578.
Kostiainen, M.A., Hiekkataipale, P., Laiho, A., Lemieux, V., Seitsonen, J., Ruokolainen, J., Ceci, P., 2013. Electrostatic assembly of binary nanoparticle superlattices using protein cages. Nat. Nanotechnol. 8 (1), 52–56. https://doi.org/10.1038/nnano.2012.220.
Ksenofontov, A.L., Dobrov, E.N., Fedorova, N.V., Serebryakova, M.V., Prusov, A.N., Baratova, L.A., Paalme, V., Järvekülg, L., Shtykova, E.V., 2018. Isolated potato virus A coat protein possesses unusual properties and forms different short virus-like particles. J. Biomol. Struct. Dyn. 36 (7), 1728–1738. https://doi.org/10.1080/07391102.2017.1333457.
Lee, S.W., Wood, B.M., Belcher, A.M., 2003. Chiral smectic C structures of virus-based films. Langmuir 19 (5), 1592–1598. https://doi.org/10.1021/la026387w.
Lee, B., Lo, C.T., Thiyagarajan, P., Winans, R.E., Li, X., Niu, Z., Wang, Q., 2007. Effect of interfacial interaction on the cross-sectional morphology of tobacco mosaic virus using GISAXS. Langmuir 23 (22), 11157–11163. https://doi.org/10.1021/la7009989.
Lee, L.A., Niu, Z., Wang, Q., 2009. Viruses and virus-like protein assemblies-chemically programmable nanoscale building blocks. Nano Res. 2 (5), 349–364. https://doi.org/10.1007/s12274-009-9033-8.
Li, C., Evans, J., Wang, N., Guo, T., He, S., 2019. PH dependence of the chirality of nematic cellulose nanocrystals. Sci. Rep. 9 (1), 1–7. https://doi.org/10.1038/s41598-019-47834-w.
Liljeström, V., Ora, A., Hassinen, J., Rekola, H.T., Nonappa, N., Heilala, M., Hynninen, V., Joensuu, J.J., Ras, R.H.A., Törmä, P., Ikkala, O., Kostiainen, M.A., 2017. Cooperative colloidal self-assembly of metal-protein superlattice wires. Nat. Commun. 8 (1), 1–10. https://doi.org/10.1038/s41467-017-00697-z.
Linko, V., Zhang, H., Nonappa, Kostiainen, M.A., Ikkala, O., 2022. From precision colloidal hybrid materials to advanced functional assemblies. Acc. Chem. Res. 55 (13), 1785–1795. https://doi.org/10.1021/acs.accounts.2c00093.
Lu, B., Stubbs, G., Culver, J.N., 1996. Carboxylate interactions involved in the disassembly of tobacco mosaic tobamovirus. Virology 225 (1), 11–20. https://doi.org/10.1006/viro.1996.0570.
Martí, M., Merwaiss, F., Butković, A., Daròs, J.-A., 2022. Production of potyvirus-derived nanoparticles decorated with a nanobody in biofactory plants. Front. Bioeng. Biotechnol. 10, 502. https://doi.org/10.3389/fbioe.2022.877363.
Martínez-Turiño, S., García, J.A., 2020. Potyviral coat protein and genomic RNA: a striking partnership leading virion assembly and more. In: Advances in Virus Research, vol. 108. Academic Press, pp. 165–211. https://doi.org/10.1016/bs.aivir.2020.09.001.
Moghimian, P., Srot, V., Rothenstein, D., Facey, S.J., Harnau, L., Hauer, B., Bill, J., Van Aken, P.A., 2014. Adsorption and self-assembly of M13 phage into directionally organized structures on C and SiO_2 films. Langmuir 30 (38), 11428–11432. https://doi.org/10.1021/la502534t.
Murphy, C.J., Sau, T.K., Gole, A.M., Orendorff, C.J., Gao, J., Gou, L., Hunyadi, S.E., Li, T., 2005. Anisotropic metal nanoparticles: synthesis, assembly, and optical applications. J. Phys. Chem. B 109 (29), 13857–13870. https://doi.org/10.1021/jp0516846.
Nault, L., Taofifenua, C., Anne, A., Chovin, A., Demaille, C., Besong-Ndika, J., Cardinale, D., Carette, N., Michon, T., Walter, J., 2015. Electrochemical atomic force microscopy imaging of redox-immunomarked proteins on native potyviruses: from subparticle to single-protein resolution. ACS Nano 9 (5), 4911–4924. https://doi.org/10.1021/acsnano.5b00952.
Nie, Z., Kumacheva, E., 2008. Patterning surfaces with functional polymers. Nat. Mater. 7 (4), 277–290. https://doi.org/10.1038/nmat2109.
Niu, Z., Bruckman, M., Kotakadi, V.S., He, J., Emrick, T., Russell, T.P., Yang, L., Wang, Q., 2006. Study and characterization of tobacco mosaic virus head-to-tail assembly assisted by aniline polymerization. Chem. Commun. 28, 3019–3021. https://doi.org/10.1039/b603780a.
Park, S.M., Kim, W.G., Kim, J., Choi, E.J., Kim, H., Oh, J.W., Yoon, D.K., 2021. Fabrication of chiral M13 bacteriophage film by evaporation-induced self-assembly. Small 17 (26), 2008097. https://doi.org/10.1002/smll.202008097.
Plummer, E.M., Manchester, M., 2011. Viral nanoparticles and virus-like particles: platforms for contemporary vaccine design. Wiley Interdiscip. Rev. Nanomedicine Nanobiotechnology 3 (2), 174–196. https://doi.org/10.1002/wnan.119.
Pogostin, B.H., Malmendal, A., Londergan, C.H., Åkerfeldt, K.S., 2019. PKA determination of a histidine residue in a short peptide using Raman spectroscopy. Molecules 24 (3), 405. https://doi.org/10.3390/molecules24030405.
Pokorski, J.K., Steinmetz, N.F., 2011. The art of engineering viral nanoparticles. Mol. Pharm. 8 (1), 29–43. https://doi.org/10.1021/mp100225y.
Puetz, J., Aegerter, M.A., 2004. Dip coating technique. In: Sol-Gel Technologies for Glass Producers and Users. Springer US, pp. 37–48. https://doi.org/10.1007/978-0-387-88953-5_3.
Rink, V., Müller-Renno, C., Ziegler, C., Braun, M., Boonrod, K., Krczal, G., 2017. Electrostatic conditions define the 2D self-assembly of tomato bushy stunt viruses on solid surfaces. Biointerphases 12 (4), 04E402. https://doi.org/10.1116/1.4986055.
Rong, J., Niu, Z., Lee, L.A., Wang, Q., 2011. Self-assembly of viral particles. Curr. Opin. Colloid Interface Sci. 16 (6), 441–450. https://doi.org/10.1016/j.cocis.2011.09.001.
Santos, J.L.R., Bispo, J.A.C., Landini, G.F., Bonafe, C.F.S., 2004. Proton dependence of tobacco mosaic virus dissociation by pressure. Biophys. Chem. 111 (1), 53–61. https://doi.org/10.1016/j.bpc.2004.04.003.
Shtykova, E.V., Petoukhov, M.V., Fedorova, N.V., Arutyunyan, A.M., Skurat, E.V., Kordyukova, L.V., Moiseenko, A.V., Ksenofontov, A.L., 2021. The structure of the potato virus A particles elucidated by small angle X-ray scattering and complementary techniques. Biochemist 86 (2), 230–240. https://doi.org/10.1134/S0006297921020115.
Smith, M.T., Hawes, A.K., Bundy, B.C., 2013. Reengineering viruses and virus-like particles through chemical functionalization strategies. Curr. Opin. Biotechnol. 24 (4), 620–626. https://doi.org/10.1016/j.copbio.2013.01.011.
Sulczewski, F.B., Liszbinski, R.B., Romão, P.R.T., Rodrigues Junior, L.C., 2018. Nanoparticle vaccines against viral infections. Arch. Virol. 163 (9), 2313–2325. https://doi.org/10.1007/S00705-018-3856-0.
Thanh, N.T.K., Green, L.A.W., 2010. Functionalisation of nanoparticles for biomedical applications. Nano Today 5 (3), 213–230. https://doi.org/10.1016/j.nantod.2010.05.003.
Thorkelsson, K., Bai, P., Xu, T., 2015. Self-assembly and applications of anisotropic nanomaterials: a review. Nano Today 10 (1), 48–66. https://doi.org/10.1016/j.nantod.2014.12.005.
Tseng, R.J., Tsai, C., Ma, L., Ouyang, J., Ozkan, C.S., Yang, Y., 2006. Digital memory device based on tobacco mosaic virus conjugated with nanoparticles. Nat. Nanotechnol. 1 (1), 72–77. https://doi.org/10.1038/nnano.2006.55.
Valli, A., García, J.A., López-Moya, J., 2015. J. Potyviridae. In *eLS*. John Wiley & Sons, Ltd, pp. 1–10. https://doi.org/10.1002/9780470015902.a0000755.pub3.
Wargacki, S.P., Pate, B., Vaia, R.A., 2008. Fabrication of 2D ordered films of tobacco mosaic virus (TMV): processing morphology correlations for convective assembly. Langmuir 24 (10), 5439–5444. https://doi.org/10.1021/la7040778.
Yoo, S.Y., Chung, W.J., Kim, T.H., Le, M., Lee, S.W., 2011. Facile patterning of genetically engineered M13 bacteriophage for directional growth of human fibroblast cells. Soft Matter 7 (2), 363–368. https://doi.org/10.1039/c0sm00879f.
Zhao, X., Lin, Y., Wang, Q., 2015. Virus-based scaffolds for tissue engineering applications. Wiley Interdiscip. Rev. Nanomedicine Nanobiotechnology 7 (4), 534–547. https://doi.org/10.1002/WNAN.1327.